

Coherent-states dynamics of the $\text{H}^+ + \text{HF}$ reaction at $E_{\text{Lab}} = 30$ eV: A complete electron nuclear dynamics investigation

Buddhadev Maiti ^a, Raymond Sadeghi ^b, Anthony Austin ^a, Jorge A. Morales ^{a,*}

^a Department of Chemistry and Biochemistry, Texas Tech University, P.O. Box 41061, Lubbock, TX 79409-1061, USA

^b Department of Chemistry, University of Texas at San Antonio, One UTSA Circle, San Antonio, TX 78249-0698, USA

Received 17 May 2007; accepted 24 July 2007

Available online 3 August 2007

Abstract

Results of a complete investigation of the $\text{H}^+ + \text{HF}$ reaction at $E_{\text{Lab}} = 30$ eV with the electron nuclear dynamics (END) and the coherent-states dynamics (CSD) theories are herein presented. Current END–CSD methodology employs frozen Gaussian wave packet in the semiclassical limit of $\hbar \rightarrow 0$ for the nuclei, and a single-determinantal Thouless coherent state (CS) for the electrons. The simulated 400 CS trajectories from five independent HF target orientations provide a complete description of the reactive processes in this system, including: non-charge-transfer scattering (NCTS), charge-transfer scattering (CTS), hydrogen fluoride dissociation (H–F D), and hydrogen rearrangement (HR). Several aspects of the reactions dynamics, such as mechanistic details and rainbow angles effects, are discussed. Differential and integral cross sections are evaluated via a novel CS formulation of those properties in conjunction with semiclassical techniques. The calculated total differential cross section shows an excellent agreement with available experimental results.

© 2007 Elsevier B.V. All rights reserved.

Keywords: Coherent states theory; Proton–molecule collisions; Scattering

1. Introduction

The study of non-charge-transfer and charge-transfer reactions in gas-phase ion–molecule collisions is of primary importance for both theoretical and applied chemistry. The relevance of those reactions are easy to recognize from their astonishing ubiquity in plasmas, particle accelerators, flames, fusion processes, upper atmosphere reactions, and astrophysical phenomena, *inter alia*. Unsurprisingly, a large amount of data concerning ion–atom collisions have become available from scattering experiments at high (hyperthermal) collisional energies (>10 keV) and several theoretical methods have been developed to interpret and predict those measurements [1]. Due mostly to technical difficulties, there have been fewer scattering experiments involving ion–molecule collisions at low (thermal) and/or intermediate (10–1000 eV) collisional energies, as is the

case of the reactive system investigated herein. That situation is somewhat regrettable because those lower collisional energies are more characteristic of genuine chemical processes.

Although several types of ion projectiles have been employed to probe molecular targets, protons possess a unique combination of properties that makes them quite suitable for scattering studies. For instance, a proton projectile has no structure and therefore cannot undergo itself inelastic rovibrational transitions during a collision but instead can cause and confine those phenomena on its collisional counterpart. In addition, a proton projectile has a very low mass, a property that renders short collisional times, facilitates inelastic processes on the target, simplifies the post-collision kinematical interpretation of angular distributions, and enhances energy-loss resolution. More importantly, a proton projectile can readily gain one electron from a molecular target and thus probe charge-transfer reactions. Due to those advantages, a large number of proton–molecule reactions engaging several types of molecular

* Corresponding author. Tel.: +1 806 742 3094; fax: +1 806 742 1289.
E-mail address: jorge.morales@ttu.edu (J.A. Morales).

targets have been investigated via scattering experiments in the last decades. The variety of those experiments is so vast that certainly defies any attempt at reviewing but still a few representative experiments, relevant to the present investigation, can be reported for sake of illustration. For instance, several research groups have meticulously investigated the $H^+ + H_2$ system because it is one of the simplest still displaying a full range of chemical processes such as rovibrational excitation, rearrangement, dissociation, non charge-transfer and charge-transfer reactions. Consequently, Udseth et al. [2] investigated transition probabilities and differential cross sections for vibrational excitations in collisions of H^+ with H_2 and with its isotopic variants HD and D_2 ; Schinke et al. [3] reported differential cross sections for vibrational excitations in the $H^+ + H_2$ reaction at collision energies of 15.3 and 20 eV; Schmidt et al. [4] provided a detailed account of rotational and vibrational scattering processes and of angular distributions of individual rotational transitions in the $H^+ + H_2$ system at collision energies of 4.67 and 6 eV; Hermann et al. [5] measured rotationally resolved vibrational excitations in $H^+ + H_2$ at the collision energy of 10 eV; and Krutein et al. [6] measured the vibrational excitation of a H_2 molecular target by H^+ impact at a scattering angle of 0° in the energy range of 15–120 eV. Obviously, proton–molecule studies have been not limited to H_2 targets and several research groups have systematically probed more complex molecular targets. Out of many examples in the literature, studies concentrating on hydrocarbon targets may be briefly mentioned herein because of their obvious chemical significance. For instance, Kusakabe et al. [7] combined experimental and theoretical results to investigate charge-transfer processes in the reactions of H^+ projectiles with H_2 , CH_4 , C_2H_2 , C_2H_6 and C_3H_8 molecular targets in the collision energy range of 0.2–4.0 keV; Cheng and Liu [8] measured total differential cross sections for different types of charge-transfer processes in the $H^+ + C_2H_2$ system at the collision energies of 6, 12.5, 25 and 50 keV; Sanders et al. [9] measured electron-capture cross sections of H^+ projectiles colliding with H_2 , CH_4 , C_2H_2 , C_2H_4 , C_2H_6 , C_3H_6 and C_3H_8 molecular targets in the energy range of 60–120 keV; Varghese et al. [10] measured total single-electron-capture cross sections of H^+ projectiles colliding with CH_4 , C_2H_2 , C_2H_4 , C_2H_6 , $(CH_2)_3$, C_3H_6 , C_3H_8 , CO , CO_2 , O_2 , CF_4 , C_2F_6 , C_4F_8 , SF_6 and Ne molecular targets in the collision energy range of 0.8–3.0 MeV; and Wilson and Toburen [11] investigated the reactions of H^+ projectiles with CH_4 , C_2H_6 , C_2H_4 , C_2H_2 and C_6H_6 molecular targets at the collision energies of 0.3, 1.0 and 2.0 MeV.

Out of the several proton-scattering experiments found in the literature, those conducted by the Toennies group [12–19] have provided the most detailed investigations on non-charge-transfer and charge-transfer reactions in proton–molecule collisions. Toennies group apparatus in those experiments consisted of a primary beam of protons in the collision energy range of $10 \leq E_{Lab} \leq 46$ eV and colliding with a secondary nozzle beam of target molecules; the par-

ticles produced by that two-beam collision (scattered protons and hydrogen atoms in non-charge-transfer and charge-transfer reactions, respectively) were subsequently measured and time-of-flight analyzed via an open electron multiplier detector. Toennies group experiments on proton–molecule collisions have systematically probed an astonishing number of molecular targets including: H_2 [12], O_2 [13], HF [14], H_2O [15], CO_2 [16], N_2O [16], C_2H_2 [17], CF_4 [18], SF_6 [18], and CH_4 [19] *inter alia*. Worth noticing in that series of experiments were the measurements of non-charge-transfer and charge-transfer vibrationally resolved differential cross sections in the systems: $H^+ + H_2$ at $E_{Lab} = 30$ eV [12] and $H^+ + O_2$ at $E_{Lab} = 23.7$ eV [13]; and the measurements of non-charge-transfer and charge-transfer total differential cross sections in the systems: $H^+ + CO_2$ and $H^+ + N_2O$ at $E_{Lab} = 9.8$ eV and 30 eV [16], $H^+ + H_2O$ at $E_{Lab} = 27$ and 46 eV [15], and $H^+ + C_2H_2$ at $E_{Lab} = 30$ eV [17].

Toennies group studies have set the stage for a productive interaction between experimental and theoretical approaches because its measurements can be used to assess the accuracy of a given theoretical method whereas the latter can elucidate reaction details not accessible by experimental means. However, due to the complexity of the investigated proton–molecule reactions, few of them have been studied theoretically with advanced quantum methodologies. An early attempt in that direction was made by Toennies et al. themselves when they simulated their own $H^+ + H_2$ experiment [12], first with the trajectory surface hopping method (TSHM) [12,20] and finally with the higher-level infinite order sudden approximation (IOSA) method [21]. However, the possibility to theoretically examine the most demanding Toennies experiments arose when Morales et al. applied systematically the electron nuclear dynamics (END) theory [22] to the reactions: $H^+ + H_2$ [23,24], $H^+ + CH_4$ [25], and $H^+ + H_2O$ [26], and obtained excellent agreements with the corresponding Toennies group's measurements. The success of END in simulating those systems is attributable to two distinctive features of that theory: (I) its direct-dynamics nature that makes possible its application to different types of systems without the cumbersome predetermination of potential energy surfaces, and (II) its intrinsic versatility that permits the description of different types of reactions occurring in the above systems (e.g. hydrogen rearrangements, hydrogen dissociations, charge-transfer processes, etc.). Encouraged by those early results, we continued applying the END theory to more complex systems experimentally studied by the Toennies group but now in the context of our generalized coherent-states dynamics (CSD) (see next section for details). For example, we have recently completed an exhaustive study [27] on the proton–acetylene collision: $H^+ + CH \equiv CH$ at $E_{Lab} = 30$ eV [28] that involved the simulation of 6800 trajectories from 68 independent $HC \equiv CH$ target orientations, rendered a complete description of all the reactive processes in that system (e.g. H_2 formation and charge-transfer reactions), and provided calculated

cross sections in good agreement with experimental results (see also Ref. [29] for a complementary END study on the same system). Other example of our current research efforts is our ongoing END–CSD theoretical study [30] of the $H^+ + CO_2$ system at $E_{Lab} = 30$ eV [16] with an emphasis on quantitatively describing the non-charge-transfer $H^+ + CO_2 \rightarrow H^+ + CO_2$ and charge-transfer $H^+ + CO_2 \rightarrow H + CO_2^+$ channels of that system. In the same vein, we present herein a detailed END–CSD study of the $H^+ + HF$ reaction at $E_{Lab} = 30$ eV that was also experimentally studied by the Toennies group [14]. This reactive system displays a wealth of fascinating chemical features that call for a detailed theoretical investigation. Firstly, this system exhibits several chemical processes such as proton inelastic scattering, target vibrational excitations, and charge-transfer reactions. Secondly, the possibility of theoretically predicting the formation of H_2F^+ , a compound independently identified in infrared laser spectroscopy [31,32], gives a further stimulus for a theoretical investigation. Finally, unlike other previously investigated molecular targets (e.g. H_2 [23,24], $H-C\equiv C-H$ [27], and CO_2 [30]), the HF molecule has no inversion center and therefore presents an electronic density with some degree of asymmetry between the H and the F termini; this lack of symmetry has an effect on the interacting forces between the HF target and the incoming/outgoing projectile that finally manifests in a more varied dynamics and in more complex patterns in the scattering angle functions. It should be finally emphasized that the mentioned direct-dynamics nature of END–CSD happens to be crucial in this investigation because there is no pre-calculated potential energy surface for the $H^+ + HF$ system to undertake such a study with more traditional, non-direct methods. As proven in a previous study of the $H^+ + H_2$ system [23,24], direct-dynamics results with END compare well with those generated on potential energy surfaces with the TSHM [12] and IOSA [21] methods.

The present investigation is organized as follows: in Section 2, we discuss the END–CSD theory as the current methodology to study the $H^+ + HF$ system; in Section 3, we explain the computational details of the present END–CSD simulations; in Section 4, we report and discuss the main END–CSD results for the $H^+ + HF$ system; and finally in Section 5, we present some final and concluding remarks.

2. Theoretical background

The END theory has been created by Deumens and Öhrn [22]. In this investigation, we present END in the context of our unifying coherent-states dynamics (CSD) theory [33] that prescribes specific types of coherent states (CS) for each class of molecular degree of freedom: translational, rotational, vibrational, and electronic. The utilization of CS for the simulation of chemical reactions arises from both theoretical and computational motivations but the last one is of paramount importance for the feasibility

of the present approach. Even with state-of-the-art computer technology, full quantum-mechanics simulations of large chemical systems remain unfeasible and recurrences to less expensive classical-mechanics treatments are inescapable in some degrees of freedom. Therefore, a practical methodology to treat large systems would be one that allows transitions from quantum to classical mechanics in a continuous way and at any desired level of accuracy. Such flexibility can be obtained by exploiting the properties of CS sets [34]. Broadly speaking, CS are sets of genuine quantum states that permit expressing full quantum dynamical equations in a classical-like Hamiltonian format (symplectic structure [35,36]) in terms of generalized positions $\{q_i\}$ and conjugate momenta $\{p_i\}$. More formally speaking, the states $\{|z_i\rangle\}$, depending upon the complex parameters $z_i = (q_i + ip_i)/\sqrt{2}$, form a set of CS in the Hilbert space \mathbf{H} if they satisfy the following two conditions [34]: (I) continuity with respect to z_i , and (II) resolution of unity: $\hat{1} = \int d\mu(z_i, z_i^*) |z_i\rangle \langle z_i|$ with positive measure $d\mu(z_i, z_i^*) > 0$ and with $\langle z_i | z_i^* \rangle \neq 0$ (i.e. the CS form a non-orthogonal, over-complete basis set [34]). Some types of CS sets also satisfy additional conditions [34] but only that concerning a quasi-classical behavior [37] is relevant herein. A CS set is termed quasi-classical [37] if the CS average positions and momenta are $\langle \hat{x}_i \rangle = q_i(t) = \langle z_j(t) | \hat{x}_i | z_j(t) \rangle$ and $\langle \hat{p}_i \rangle = p_i(t) = \langle z_j(t) | \hat{p}_i | z_j(t) \rangle$, respectively, and there exists a Hamiltonian \hat{H} with which those averages evolve in time obeying Hamilton equations: $\dot{q}_i = \partial H(q_i, p_i) / \partial p_i$ and $\dot{p}_i = -\partial H(q_i, p_i) / \partial q_i$, where $H(q_i, p_i) = \langle z_j(t) | \hat{H} | z_j(t) \rangle$. If a CS set is used to formulate equations of motion then the resulting dynamics will still be genuinely quantum-mechanical but cast in a classical-like format as close to classical mechanics as possible; if the CS sets are also quasi-classical then a classical dynamics obeyed by quantum states is obtained. Most of the CS herein described can be constructed via the Lie-group Perelomov prescription (PP), whose intricate details are explained in Ref. [34]. However, the PP does not automatically generate quasi-classical CS. Non-trivial departures from the PP to enforce quasi-classical CS behavior are demonstrated in Ref. [37]. Additionally, a less strict version of the second CS condition is discussed in Refs. [34,37].

For a molecular system with N_N nuclei and N_e electrons, the simplest END–CSD total wavefunction Ψ_{Total} is the product of nuclear Ψ_N and electronic Ψ_e parts: $\Psi_{Total} = \Psi_N \Psi_e$. Ψ_N is a product of $3N_N$ narrow-width, frozen Gaussian wave packets:

$$\Psi_N(\mathbf{X}; \mathbf{R}, \mathbf{P}) = \prod_{i=1}^{3N_N} \exp \left\{ - \left(\frac{X_i - R_i}{2\Delta R_i} \right)^2 + \frac{iP_i}{\hbar} (X_i - R_i) \right\} \quad (1)$$

with average positions R_i , average momenta P_i , and position normal deviation $\Delta R_i \propto \hbar^{1/2}$. These Gaussian wave packets are Glauber CS [24] in themselves. In a CSD approach [33], Ψ_N can be approximately factorized into translational, rotational and vibrational CS parts:

$\Psi_N = \Psi_{\text{Trans}} \Psi_{\text{Rot}} \Psi_{\text{Vib}} \Psi_{\text{Trans}}$ is a collection of CS wave packet describing quasi-classically the center of mass motion and the reactants/products relative motions [33,37]. Ψ_{Rot} is approximately the nearly quasi-classical Morales rotational CS $\Psi_{\text{Rot}} = |\alpha\beta\gamma\rangle$ [37] generated by a departure from the PP treatment of the $SO(3) \otimes SO(3) \otimes A$ Lie group. Ψ_{Vib} is a product of N_{Vib} normal-mode, quasi-classical Glauber CS [24]: $\Psi_{\text{Vib}} = \prod_{i=1}^{N_{\text{Vib}}} |z_i^{\text{Vib}}\rangle$. The approximate nature of this CS factorization is due to the fact that Ψ_{Rot} is not strictly Gaussian in form [33,37] unlike the other CS factors. A full CSD treatment should involve the discussed CS factorization throughout the whole dynamics. However, for the present application, the original END form of Ψ_N in Eq. (1) is adopted and the CS factorization is only introduced at final time to perform a CS analysis of the final state. For Ψ_e , K fermion creation (annihilation) operators $b_i^\dagger(b_i)$ of N_e occupied $\{\psi_h\}$ and $K - N_e$ virtual $\{\psi_p\}$ orthogonal molecular spin-orbitals (MSO) can generate particle-hole pair operators $b_p^\dagger b_h$ of the $U(K)$ Lie group [34]. Taking as a fiducial state the Fermi vacuum $|0\rangle = b_{N_e}^\dagger \cdots b_1^\dagger |\text{vac}\rangle$, the un-normalized, non-quasi-classical, single-determinant Thouless electronic CS [34,38] $|\mathbf{z}; \mathbf{R}\rangle$ is

$$\begin{aligned} \Psi_e = |\mathbf{z}; \mathbf{R}\rangle &= \det[\chi_h(\mathbf{z}; \mathbf{R})] = \exp\left(\sum_{p=N_e+1}^K \sum_{h=1}^{N_e} z_{ph} b_p^\dagger b_h\right) |0\rangle \\ &= |0\rangle + \sum_{p,h} z_{ph}(t) b_p^\dagger b_h |0\rangle + \sum_{p,h,p',h'} z_{ph}(t) z_{p'h'}(t) b_p^\dagger b_{p'}^\dagger b_{h'} b_h |0\rangle + \cdots, \end{aligned} \quad (2)$$

where the non-orthogonal Thouless (or dynamical) MSO $\{\chi_h\}$ are $\chi_h = \psi_h + \sum_{p=N_e+1}^K \psi_p z_{ph}$ ($1 \leq h \leq N_e$) [38] and $b_p^\dagger b_h |0\rangle$, $b_p^\dagger b_{p'}^\dagger b_{h'} b_h |0\rangle$, etc., are singly-, doubly-excited, etc., determinants out of $|0\rangle$. The $\{\psi_h, \psi_p\}$ MSO are constructed with conventional atomic basis set functions centered on the nuclear wave packets and therefore they depend upon $\{R_i\}$ and so does $|\mathbf{z}; \mathbf{R}\rangle$. Those MSO are unrestricted so that $|\mathbf{z}; \mathbf{R}\rangle$ can in principle describe both closed-shell $H^+ + HF$ and open-shell $H^o + HF^+$ separations. Thouless CS plays several roles in the present formulation. Basically, Thouless theorem [38] certifies that $|\mathbf{z}; \mathbf{R}\rangle$ is any general single determinant, non-orthogonal to and out of $|0\rangle$, and defined non-redundantly in terms of the minimum number of parameters $\{z_{ph}\}$ necessary to express a single-determinantal state. Therefore, (I) $|\mathbf{z}; \mathbf{R}\rangle$ always remains single-determinantal during any arbitrary variations of $\{z_{ph}(t)\}$ without the need of holonomic constraints, and (II) $|\mathbf{z}; \mathbf{R}\rangle$ is simultaneously one single determinant in terms of the Thouless MSO $\{\chi_h\}$ and a superposition of all the excited determinants out of $|0\rangle$ in terms of the original MSO $\{\psi_h, \psi_p\}$. Those excited single-determinant can represent different non-charge-transfer and charge-transfer channels. $|\mathbf{z}; \mathbf{R}\rangle$ also permits a classical-like formulation of the quantum electronic dynamics as shown shortly. A multi-configuration electronic CS [39] would be more adequate to describe the multi-channel $H^+ + HF$ reaction but has not been implemented yet. Nevertheless, the present single-determinantal Thouless CS comprising singly- and higher-excited

single determinants renders satisfactory results as shown below.

Having formulated Ψ_{Total} in terms of CS parts, the quantum Lagrangian L_{CS} [36] for such an un-normalized trial function is

$$L_{\text{CS}} = \left\langle \Psi_{\text{Total}} \left[\frac{i\hbar}{2} \left(\frac{\vec{\partial}}{\partial t} - \frac{\overleftarrow{\partial}}{\partial t} \right) - \hat{H} \right] \Psi_{\text{Total}} \right\rangle / \langle \Psi_{\text{Total}} | \Psi_{\text{Total}} \rangle. \quad (3)$$

By applying the time-dependent variational principle (TDVP) that imposes stationarity to the quantum action S_{CS} associated with the quantum Lagrangian: $\delta S_{\text{CS}} = \delta \int_{t_1}^{t_2} L_{\text{CS}}(t) dt = 0$ [22,36], the END dynamical equations for the CS parameters $\{R_i, P_i, z_{ph}, z_{ph}^*\}$ in the semiclassical limit of $\hbar \rightarrow 0$ for the nuclei are obtained [22,36]:

$$\begin{bmatrix} i\mathbf{C} & \mathbf{0} & i\mathbf{C}_{\mathbf{R}} & \mathbf{0} \\ \mathbf{0} & -i\mathbf{C}^* & -i\mathbf{C}_{\mathbf{R}}^* & \mathbf{0} \\ i\mathbf{C}_{\mathbf{R}}^\dagger & -i\mathbf{C}_{\mathbf{R}}^\dagger & \mathbf{C}_{\mathbf{RR}} & -\mathbf{I} \\ \mathbf{0} & \mathbf{0} & \mathbf{I} & \mathbf{0} \end{bmatrix} \begin{bmatrix} \frac{dz}{dt} \\ \frac{dz^*}{dt} \\ \frac{d\mathbf{R}}{dt} \\ \frac{d\mathbf{P}}{dt} \end{bmatrix} = \begin{bmatrix} \frac{\partial E_{\text{Total}}}{\partial z^*} \\ \frac{\partial E_{\text{Total}}}{\partial z} \\ \frac{\partial E_{\text{Total}}}{\partial \mathbf{R}} \\ \frac{\partial E_{\text{Total}}}{\partial \mathbf{P}} \end{bmatrix}, \quad (4)$$

where the left matrix is related to a Hamilton generalized symplectic matrix [35,36] whose sub-matrices are:

$$\begin{aligned} (\mathbf{C}_{\mathbf{XY}})_{ij,kl} &= -2\text{Im} \frac{\partial^2 \ln S}{\partial X_{ik} \partial Y_{jl}} \Big|_{\mathbf{R}'=\mathbf{R}}; \\ (\mathbf{C}_{\mathbf{Xik}})_{\text{ph}} &= \frac{\partial^2 \ln S}{\partial z_{\text{ph}}^* \partial X_{ik}} \Big|_{\mathbf{R}'=\mathbf{R}}; \quad \mathbf{C}_{\text{ph:qg}} = \frac{\partial^2 \ln S}{\partial z_{\text{ph}}^* \partial z_{\text{qg}}} \Big|_{\mathbf{R}'=\mathbf{R}}, \end{aligned} \quad (5)$$

where $S = \langle \mathbf{z}; \mathbf{R}' | \mathbf{z}; \mathbf{R} \rangle$ is the overlap between two Thouless CS and $E_{\text{Total}} = \langle \Psi_{\text{Total}} | \hat{H} | \Psi_{\text{Total}} \rangle / \langle \Psi_{\text{Total}} | \Psi_{\text{Total}} \rangle = \sum_{i=1}^{3N_N} P_i^2 / 2M_i + \langle \mathbf{z}; \mathbf{R} | \hat{H}_e | \mathbf{z}; \mathbf{R} \rangle / \langle \mathbf{z}; \mathbf{R} | \mathbf{z}; \mathbf{R} \rangle$ the total energy. Eq. (4) expresses in a quantum Hamilton symplectic format [36] the combined quantum classic-like electronic and quasi-classical CM, rotational and vibrational CS dynamics. Remarkably, Eq. (4) treats simultaneously the electrons and nuclei of a system and provides a direct-dynamics algorithm that does not require pre-calculated potential energy surfaces to run. The CS parameters evolving in time draw different reaction trajectories in a CS quantum phase space. In a simulation, reactants are prepared with initial positions and momenta: $\{R_i^0\}$ and $\{P_i^0\}$, and with electronic state $\{z_{ph}^0, z_{ph}^{0*}\}$ (cf. Fig. 1) to define the initial wavefunction: $\Psi_{\text{Total}}^i = \Psi_{\text{Total}}^0$. At initial time, all z_{ph}^0 may be zero: $z_{ph}^0 = 0 \Rightarrow |\mathbf{z}; \mathbf{R}\rangle = |0\rangle$, so that $|0\rangle$ is an unrestricted Hartree-Fock (UHF) self-consistent field (SCF) single determinant describing the incoming $H^+ + HF$. A chemical reaction simulation is advanced by integrating Eq. (4) over time so that the evolving CS parameters $\{R_i, P_i, z_{ph}, z_{ph}^*\}$ trace a reactants-to-products trajectory in the CS quantum phase space. Eventually, the CS parameters $\{z_{ph}(t)\}$ will assume non-zero values and the excited single determinants in Eq. (2) will come up. Some of those excited determinants will correspond to non-charge-transfer outgoing channels

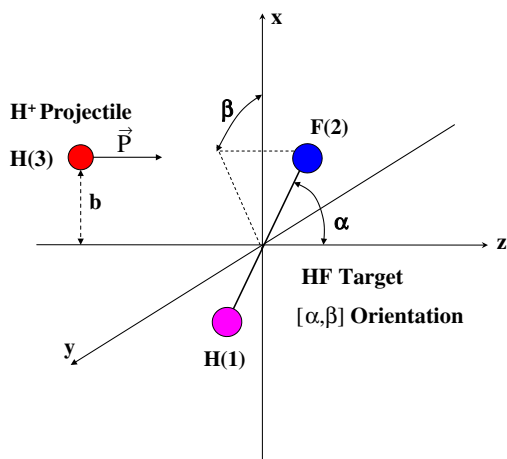


Fig. 1. $\text{H}^+ + \text{HF}$ reactants initial conditions; balls represent nuclear wave packets for the atoms with projectile impact parameter b and target orientation $[\alpha, \beta]$.

$\text{H}^+ + \text{HF}$ and others to charge-transfer ones $\text{H}^0 + \text{HF}^+$ depending upon the MSO $\{\psi_h, \psi_p\}$ implicated in the excitations. At final time, the evolved wavefunction $\Psi_{\text{Total}}^f = \Psi_{\text{Total}}^\infty$ is factorized into its nuclear CS parts and projected onto selected eigenstates of the products: $\Phi_{\text{Total}}^f = \Phi_{\text{Trans}}^f \Phi_{\text{Rot}}^f \Phi_{\text{Vib}}^f \Phi_e^f$ so that the quantum probability amplitude $T_{\text{CS}}^{i \rightarrow f}$ for the transition $\Psi_{\text{Total}}^i \rightarrow \Psi_{\text{Total}}^f$ is [33,40]

$$T_{\text{CS}}^{i \rightarrow f} = \langle \Phi_{\text{Total}}^f | \Psi_{\text{Total}}^f \rangle = A_{\text{Trans}}^{i \rightarrow f} A_{\text{Rot}}^{i \rightarrow f} A_{\text{Vib}}^{i \rightarrow f} A_e^{i \rightarrow f} \exp\left(\frac{iS_{\text{CS}}}{\hbar}\right), \quad (6)$$

where each $A_{\text{Degree}}^{i \rightarrow f} = \langle \Phi_{\text{Degree}}^f | \Psi_{\text{Degree}}^f \rangle$ (Degree = Trans, Rot, Vib, e) is a reaction transition probability amplitude per molecular degree. All relevant properties of a chemical reaction (e.g. differential and integral cross sections, rate constants) can be calculated from the probability amplitude $T_{\text{CS}}^{i \rightarrow f}$. The specific CSD way to evaluate differential and integral cross sections is deferred to Section 4, where those calculations are discussed more concretely in the context of the simulation results.

3. Computational details

All the present calculations have been conducted with the suite of programs *CSTechG* (K. Tsereteli, Y. Yan and J. A. Morales, *CSTechG*, Texas Tech University, Lubbock, Texas, 2005–2007), developed from the *ENDyne 2.7* and *2.8* codes (E. Deumens, *ENDyne: Electron Nuclear Dynamics Simulations*, Version 2 Release 8, Quantum Theory Project: University of Florida, Gainesville, FL. 32611-8435, 1997). Original features coded into *CSTechG* include a novel density functional theory (DFT)/CSD method [41] (not employed in this investigation), a CSD methodology to calculate reaction properties [33] (employed in this investigation, see below), and a compute grid implementation [42] for Microsoft Windows[®] and Red Hat Linux[®] operating systems, *inter alia*. The last capability utilizes state-of-the-art compute grid technologies [43] to run several CS

trajectories in parallel on available compute grids, such as the Texas Tech University compute grid (*TechGrid*) and the Texas Internet Grid for Research and Education (*TIGRE*). The raw simulated dynamics in this investigation are equivalent to those with the *ENDyne 2.7-2.8* code but reaction properties are evaluated with the mentioned CSD methodology.

The nuclear CS parameters defining the initial conditions of the reactants H^+ and HF for the present calculations are depicted in Fig. 1. The nuclei initially forming the HF molecule are labeled H(1) and F(2), respectively, whereas the nucleus initially in the incoming projectile H^+ is labeled H(3). In the present calculations, the relatively large pVDZ basis set [44,45] is placed on the three moving CS nuclear wave packets to construct the electronic MSO $\{\psi_h, \psi_p\}$. For the total H^+/HF system, a pVDZ basis set contains 25 contracted basis functions constructed with 56 uncontracted Gaussian functions. Previous ($\text{H}^+ + \text{H}_2$ [23,24]) and concurrent ($\text{H}^+ + \text{NO}$) studies have demonstrated the adequacy of the pVDZ basis sets for this type of dynamical simulations. The target molecule HF is initially at rest ($\mathbf{P}_{\text{H}(1)} = \mathbf{P}_{\text{F}(2)} = \mathbf{0}$), with its geometrical center placed at (0.0, 0.0, 0.0) (Fig. 1) and in its electronic ground state at the UHF-SCF/pVDZ [46] level. The angular orientation $[\alpha, \beta]$ of the HF target molecule is determined by the polar α ($0^\circ \leq \alpha \leq 180^\circ$) and azimuthal β ($0^\circ \leq \beta \leq 360^\circ$) angles of its inter-nuclear center-F semi-axis (Fig. 1). The H^+ projectile is initially placed at $(b, 0.0, -15.00$ a.u.) where b ($0 \leq b \leq +\infty$) is the impact parameter. The incoming projectile initially travels along the positive z-axis with momentum $\mathbf{P}_{\text{H}(3)}^{\text{in}} = (0.0, 0.0, +P_{\text{H}(3)z}^{\text{in}})$ corresponding to $E_{\text{Lab}} = (P_{\text{H}(3)z}^{\text{in}})^2 / 2M_{\text{H}(3)} = 30$ eV. Taking advantage of the $C_{\infty v}$ symmetry of the HF target molecule, initial conditions not replicating symmetry-equivalent trajectories can be generated by varying the angles α and β in the ranges: $0^\circ \leq \alpha \leq 180^\circ$ and $0^\circ \leq \beta \leq 180^\circ$, respectively (for instance, the $[\alpha, \beta]$ and $[\alpha, -\beta]$ orientations generate symmetry-equivalent trajectories, cf. Fig. 1). Given the considerable computational cost of a pVDZ basis set in a dynamical context, only a subset of trajectories starting from some representative target orientations $[\alpha, \beta]$ are actually calculated. Therefore, the present simulations only consist of “orthogonal” projectile–target collisions with the target at initial orientations $[90^\circ, \beta]$ with $0^\circ \leq \beta \leq 180^\circ$ in steps of $\Delta\beta = 45^\circ$, and with the projectile at impact parameters $0.0 \leq b \leq 7.9$ a.u. in steps of $\Delta b = 0.1$ a.u. so that no symmetry-equivalent trajectories are replicated. Those initial conditions generate a total of five independent target orientations and 400 CS trajectories, which make the present END–CSD/pVDZ study be the most exhaustive hitherto conducted with a $C_{\infty v}$ target (most previous studies were conducted with $D_{\infty v}$ targets, e.g. $\text{H}-\text{C}\equiv\text{C}-\text{H}$ [27], whose higher symmetry at times helped reducing the number of target orientations). The $[90^\circ, \beta]$ “orthogonal” collisions can certainly capture the main features of the $\text{H}^+ + \text{HF}$ reactions because they are the most probable collisions [$\text{Prob}(\alpha, \beta) \propto \sin \alpha$ that is maximal with $\alpha = 90^\circ$] as proven

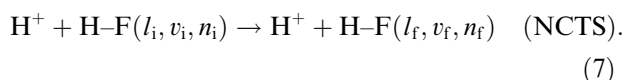
in a previous $H^+ + H-C\equiv C-H$ study [27] and corroborated in the present one. The END-CSD/pVDZ simulations were run for a total time of 1000 a.u. from the indicated initial conditions. After the simulations are complete, several programs in the *CSTechG* suite analyze the well-separated final products and calculate dynamical properties according to CSD prescriptions.

4. Results and discussion

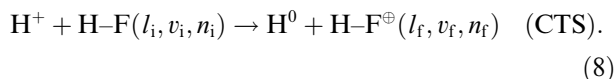
4.1. Reactive processes and trajectory analysis

The $H^+ + HF$ system at the collisional energy $E_{Lab} = 30$ eV undergoes several reactive processes. Reactions theoretically predicted during the present END-CSD/pVDZ investigation include:

- (I) Non-charge-transfer scattering (NCTS), where the incoming H^+ is scattered off after exciting the rotational, vibrational and electronic degrees of freedom of the HF molecule:

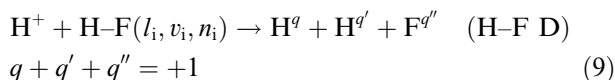


- (II) Charge-transfer scattering (CTS), where essentially one electron is transferred to the incoming projectile H^+ from the target HF:

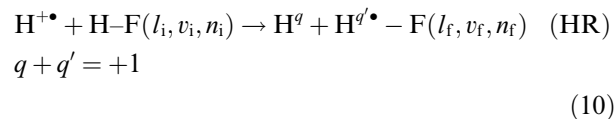


The NCTS and CTS processes happen together in a given CS trajectory with their respective probability amplitudes deducible from $A_e^{i \rightarrow f}$ in Eq. (6);

- (III) Collision-induced hydrogen fluoride dissociation (H-F D), where the HF molecule is cleaved by the incoming projectile H^+ :



- (IV) and finally hydrogen rearrangement (HR):



where the bullet ‘•’ marks the exchanged hydrogen nuclei. Neither H_2F^+ ($H^+ + HF \rightarrow H_2F^+$) nor $H_2^{+1,0}$ ($H^+ + HF \rightarrow H_2^{+1,0} + F^{0,+1}$) formation is predicted. Above, the quantum number sets: (l_i, v_i, n_i) and (l_f, v_f, n_f) label the initial and final rotational, vibrational and electronic eigenstates, respectively, because all the channels exhibit rovibrational inelasticity and electronic excitations. The CTS process directly contributes to the net one-electron charge-transfer reaction: $H^+ + HF \rightarrow H^0 + HF^+$; reciprocally, the H-F D and HR processes also contribute to that charge-transfer reaction but indirectly through the outgoing dissociated/

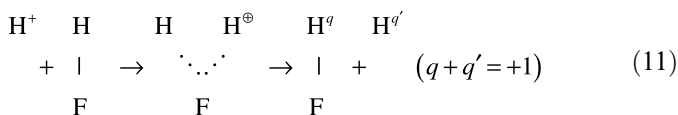
Table 1

Reactive processes per target orientation $[\alpha, \beta]$ and vs. the impact parameter b

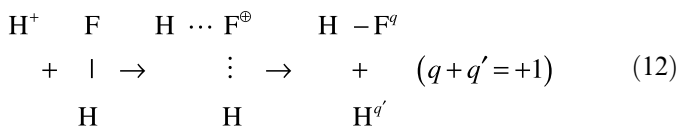
Orientation $[\alpha, \beta]$ (°)	Impact parameter, b (a.u.)	Reactive processes
[90, 0]	0.0	H-F D
	0.1–7.9	NCTS/CTS
[90, 45]	0.0–0.1	H-F D
	0.2–7.9	NCTS/CTS
[90, 90]	0.0–0.2	H-F D
	0.3–7.9	NCTS/CTS
[90, 135]	0.0–0.9	H-F D
	1.0–7.9	NCTS/CTS
[90, 180]	0.0–0.2	H-F D
	0.3–1.3	HR
	1.4–1.8	H-F D
	1.9–7.9	NCTS/CTS

NCTS, non-charge-transfer scattering; CTS, charge-transfer scattering; H-F D, hydrogen-fluoride dissociation; HR, hydrogen rearrangement.

exchanged projectile H^q having finite probability of carrying a charge $q = 0$. The complete list of all the reactive processes predicted during this END-CSD/pVDZ investigation is shown in Table 1, where the reactions are arranged first under the initial target orientations $[90^\circ, \beta]$ and then as a function of the projectile impact parameter b . Inspection of Table 1 reveals that the H-F D and HR processes occur at small values of b whereas the NCTS/CTS ones at large ones. Clearly, NCTS/CTS processes are far more probable than their more reactive counterparts: H-F D and HR. It is worth noticing that within the examined orientations, the HR reaction only arises from the $[90^\circ, 180^\circ]$ orientation; in that situation, the incoming H^+ projectile approaches the H terminus of the HF target, dislodges that H nucleus, and takes its place in the final molecule:



Although only observed from the $[90^\circ, 180^\circ]$ orientation, that type of HR mechanism will likely happen from other not simulated orientations $[\alpha, \beta]$ very close to the $[90^\circ, 180^\circ]$ one. Notably, no current simulation displays an alternative HR mechanism where the incoming H^+ projectile approaches the F terminus of the HF target, partially bonds to the F atom by weakening the original H-F bond, and finally gets bonded to the F by completely cleaving the original H-F bond:



That mechanism might happen in head-on collisions from the $[180^\circ, 0^\circ]$ orientation: $H^+ + F-H \rightarrow H \cdots F \cdots H^\oplus \rightarrow$

$\text{H}^- \text{F}^q + \text{H}^{q'} (q + q' = +1)$, whose simulations will be conducted in a future investigation.

The three main reactions in the $\text{H}^+ + \text{HF}$ system: H–F D, HR and NCTS/CTS, as predicted at the END–CSD/pVDZ level, are depicted in Figs. 2–4 for simulations starting from the target orientation $[90^\circ, 180^\circ]$ and from projectile impact parameters $b = 0.2$ (H–F D, Fig. 2), 0.9 (HR, Fig. 3), and 1.9 a.u. (NCTS/CTS, Fig. 4), respectively; and for a total time of 1000 a.u. Each of those figures breaks down into three panels: panels (a) depict the three nuclei trajectories on the x – z plane (cf. Fig. 1); panels (b) depict the relative distances between the nuclear pairs: H(1)–H(3), F(2)–H(3) and H(1)–F(2) vs. time; and panels (c) depict the Mulliken population analysis of the α -spin electrons on the nuclei: H(1), F(2) and H(3) vs. time. In all the simulations from the $[90^\circ, 0^\circ]$ and $[90^\circ, 180^\circ]$ orientations, the nuclei originally placed on the x – z plane (cf. Fig. 1) remain on that plane throughout the whole evolution due to the symmetry of the arranged atoms and of their associated interacting forces. Therefore, the 2-D panels (a) of Figs. 2–4 genuinely represent the nuclei trajec-

ries during evolution without projective distortion. From other orientations, lack of symmetry prevents the nuclei from remaining on the originally x – z plane of the initial conditions.

Fig. 2 shows a H–F D process from the $[90^\circ, 180^\circ]/b = 0.2$ a.u. initial conditions. Fig. 2a portrays the incoming projectile $\text{H}^+[\text{H}(3)]$ initially approaching the $\text{H}[\text{H}(1)]$ terminus of the HF molecule, and eventually transferring a considerable amount of momentum to the H(1) atom thereby dissociating it from the HF molecule; after that closest approach, the nuclei H(1) and H(3) depart from each other on divergent trajectories, with the nucleus H(3) violently deflected by almost 90° from its incoming direction. Notably, the much heavier fluorine nucleus F(2) remains mostly at rest during the entire processes. Fig. 2b also portrays a H–F D process since the three nuclear relative distances: H(1)–H(3), F(2)–H(3) and H(1)–F(2) initially depict the projectile–target approach but finish up being indefinitely increasing at time $t \rightarrow 1000$ a.u.; that indicates that after collision, the three nuclei diverge from each other without re-association. Fig. 2c is also consistent with H–F D and

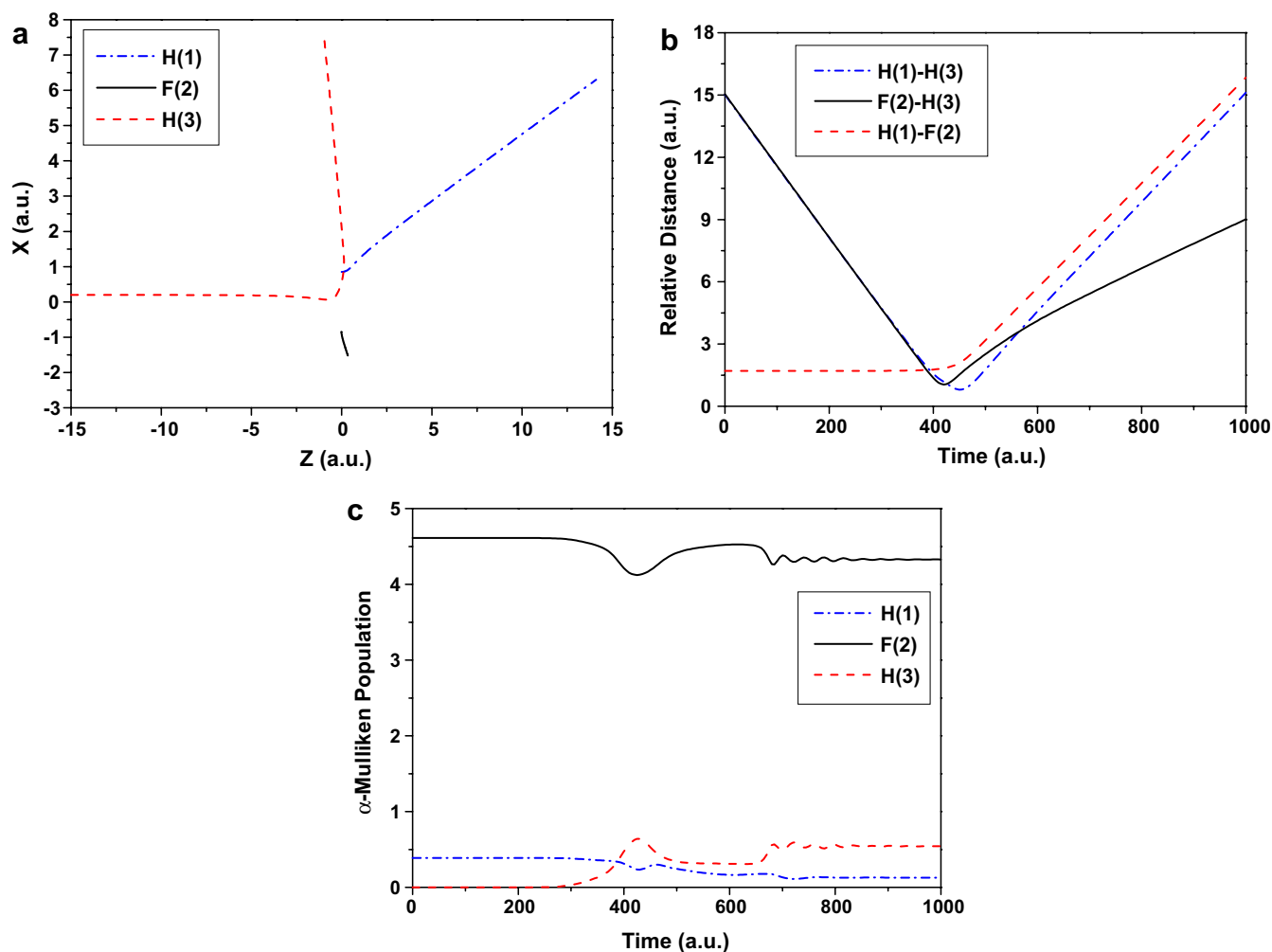


Fig. 2. Simulation of a hydrogen fluoride dissociation (H–F D) reaction in the $\text{H}^+ + \text{HF}$ system from the initial conditions: $[90^\circ, 180^\circ]/b = 0.2$ a.u. Panel (a) x vs. z positions for the three nuclei; panel (b) nuclear relative distances vs. time; panel (c) Mulliken populations of the α -spin electrons on the three nuclei vs. time.

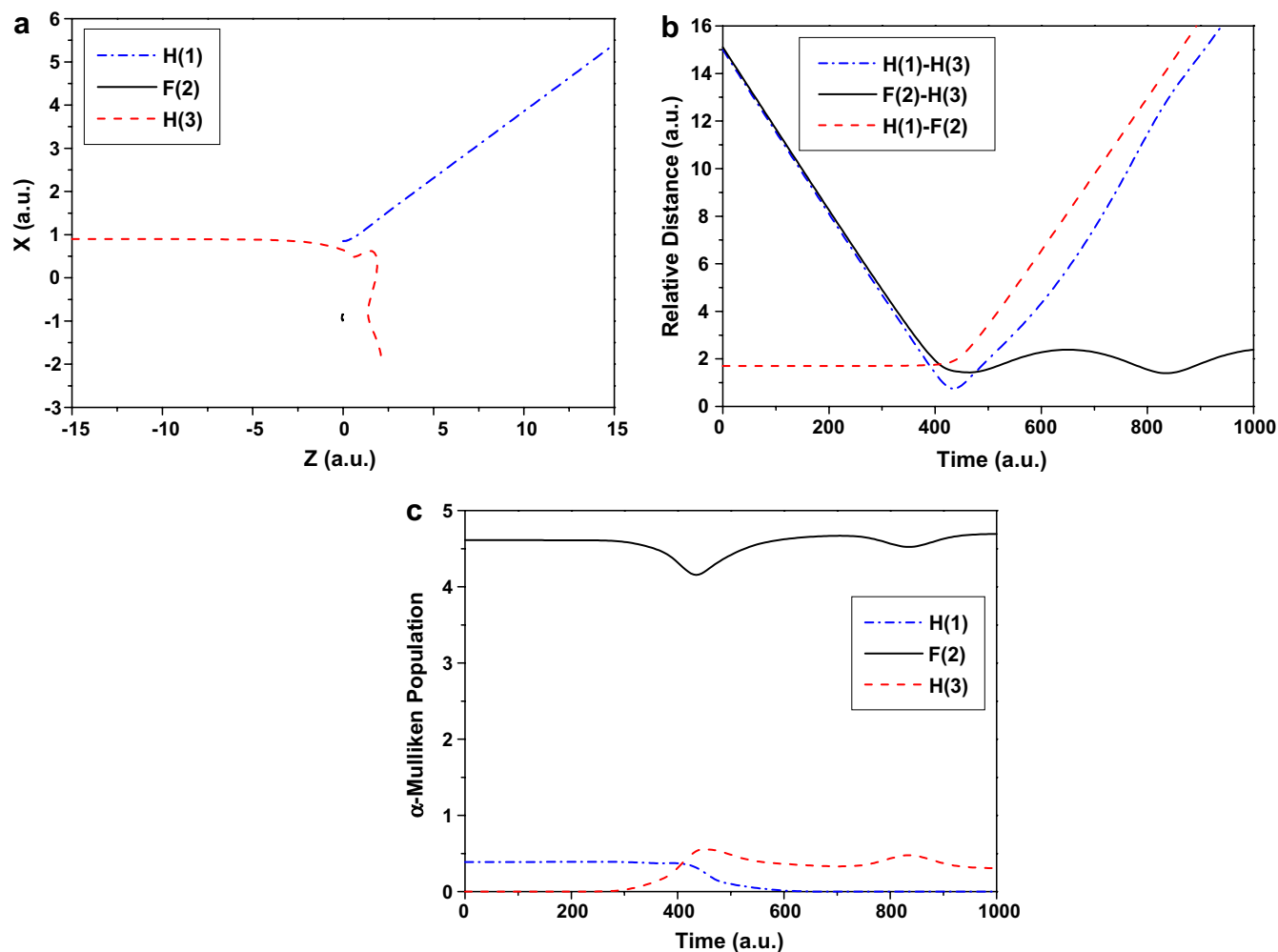


Fig. 3. Simulation of a hydrogen rearrangement (HR) reaction in the $\text{H}^+ + \text{HF}$ system from the initial conditions: $[90^\circ, 180^\circ]/b = 0.9$ a.u. Panel (a), x vs. z positions for the three nuclei; panel (b), nuclear relative distances vs. time; panel (c), Mulliken populations of the α -spin electrons on the three nuclei vs. time.

additionally illustrates the charge-transfer processes associated with it: the incoming $\text{H}^+[\text{H}(3)]$ projectile starts with no electrons but after colliding with the HF molecule, it acquires a considerable number of α -spin electrons (about $0.5\bar{e}$) at the expense of those originally in the H(1) and F(2) nuclei, whose electron populations end up proportionally decreased.

Fig. 3 shows a HR process from the $[90^\circ, 180^\circ]/b = 0.9$ a.u. initial conditions. An unmistakable discernment of that HR is achieved by inspecting simultaneously Figs. 3a and 3b. Fig. 3a depicts the incoming projectile $\text{H}^+[\text{H}(3)]$ initially approaching the H[H(1)] terminus of the HF molecule and eventually transferring a considerable amount of momentum to the H(1) nucleus so that the latter is dissociated from F(2) at the same time that H(3) orbits around and finally bonds to F(2) [cf. next Fig. 3b]; after that closest approach, the displaced H(1) nucleus is considerably deflected off. Notice again that the much heavier F(2) nucleus remains mostly at rest during the entire processes. Fig. 3b reconfirms a HR reaction for this simulation

because there the relative distance F(2)–H(1) initially remains constant at the value of the HF equilibrium bond length at the HF-SCF/pVDZ level but eventually becomes monotonically increasing at time $t \rightarrow 1000$ a.u.; on the other hand, the relative distance F(2)–H(3) initially is monotonically decreasing but finally becomes oscillatory around a constant value. Those final oscillations in the F(2)–H(3) relative distance indicates that the newly-formed HF molecule is vibrationally excited. Fig. 3c is also consistent with a HR processes and additionally illustrates the charge-transfer processes associated with it: the incoming $\text{H}^+[\text{H}(3)]$ projectile starts with no electrons but after colliding with the HF molecule, it acquires a considerable number of α -spin electrons (about $0.3\bar{e}$) at the expense of those originally in the H(1) and F(2) nuclei, whose electron populations end up proportionally decreased. The HR process displayed in Fig. 3 is a direct illustration of the HR mechanism in Eq. (11).

Fig. 4 shows a NCTS/CTS process from the $[90^\circ, 180^\circ]/b = 1.9$ a.u. initial conditions. Fig. 4a portrays the incom-

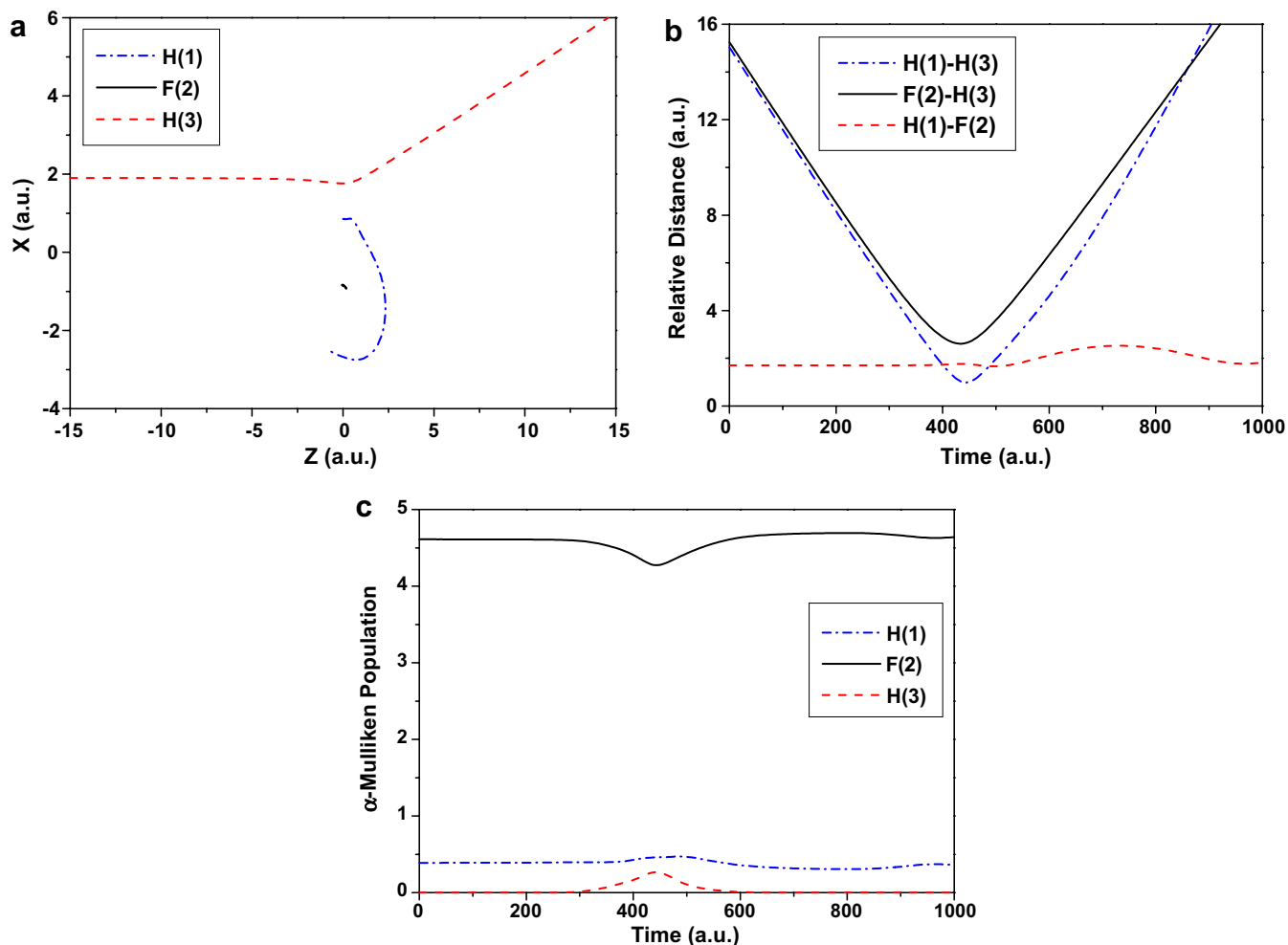


Fig. 4. Simulation of a non-charge-transfer scattering/charge-transfer scattering (NCTS/CTS) reaction in the $\text{H}^+ + \text{HF}$ system from the initial conditions: $[90^\circ, 180^\circ]/b = 1.9$ a.u. Panel (a), x vs. z positions for the three nuclei; panel (b), nuclear relative distances vs. time; panel (c), Mulliken populations of the α -spin electrons on the three nuclei vs. time.

ing projectile $\text{H}^+[\text{H}(3)]$ initially approaching the $\text{H}[\text{H}(1)]$ terminus of the HF molecule and eventually transferring a considerable amount of momentum to the $\text{H}(1)$ nucleus thereby violently pushing it back to the right and making it rotate around the slow-moving $\text{F}(2)$ nucleus; after that closest approach, the $\text{H}(3)$ nucleus is repulsively scattered off. Notice once more that the much heavier $\text{F}(2)$ nucleus remains mostly at rest during the entire processes. Fig. 4b reconfirms a NCTS/CTS reaction for this simulation because there the relative distance $\text{H}(1)\text{--}\text{F}(2)$ initially remains constant at the value of the HF equilibrium bond length at the $\text{HF}\text{-SCF/pVDZ}$ level, but eventually becomes oscillatory around the time of the $\text{H}(3)$ closest approach to the HF molecule (i.e. around the time when both $\text{F}(2)\text{--}\text{H}(3)$ and $\text{H}(1)\text{--}\text{H}(3)$ reach their minimum values), and remains in that state until time $t \rightarrow 1000$ a.u.; those oscillations indicate that the HF molecule remains bonded (and vibrationally excited) after collision. Fig. 4b also depicts the relative distances $\text{F}(2)\text{--}\text{H}(3)$ and $\text{H}(1)\text{--}\text{H}(3)$ initially decreasing monotonically (projectile–target approach) and finally reverting to a monotonic increase; that indicates that the

$\text{H}(3)$ projectile comes by and goes away from the target without causing any dissociating or rearranging process. Fig. 4c is also consistent with a NCTS/CTS reaction and additionally illustrates the charge-transfer processes associated with it: the incoming $\text{H}^+[\text{H}(3)]$ projectile starts again with no electrons but when closest to the HF molecule, it momentarily acquires a considerable number of α -spin electrons (about $0.3\bar{e}$) at the expense of those originally in the $\text{H}(1)$ and $\text{F}(2)$ nuclei, whose electron populations are momentarily decreased; that transitory electron-transfer is substantially reverted after the $\text{H}(3)$ nucleus departs from the HF molecule since it only retains a slight number of electrons at final time (fewer than $0.1\bar{e}$).

4.2. Scattering angles; rainbow and glory scattering angles

After a simulation is completed, the fastest outgoing hydrogen particle $\text{H}^q(0 \leq q \leq +1)$ is identified as the experimental outgoing projectile. The scattering angle θ of this outgoing projectile with respect to the incoming z -direction

$$\sin \theta = \frac{(P_{H_x}^{\text{out}2} + P_{H_y}^{\text{out}2})^{1/2}}{(P_{H_x}^{\text{out}2} + P_{H_y}^{\text{out}2} + P_{H_z}^{\text{out}2})^{1/2}} \quad (0 \leq \theta \leq 180^\circ), \quad (13)$$

where $\{P_{H_i}^{\text{out}}\}$ ($i = x, y, z$) are the outgoing projectile momentum components at final time. Scattering angle functions $\theta(b)$ vs. impact parameter b from the investigated initial target orientations $[\alpha, \beta]$ are shown in Fig. 5, whereas the values and locations of some of their critical values (e.g. rainbow and glory scattering angles) are listed in Table 2. The scattering angles patterns displayed in Fig. 5 differ in some details from those previously observed during similar simulations with more symmetric $D_{\infty h}$ targets (e.g. H_2 [23,24] and C_2H_2 [27]), a fact due to the lower $C_{\infty v}$ symmetry of the current HF target as discussed below.

From the $[90^\circ, 0^\circ]$, $[90^\circ, 45^\circ]$ and $[90^\circ, 90^\circ]$ orientations, the scattering angle functions $\theta(b)$ in Fig. 5 exhibit primary rainbow angles $\theta_R^{\text{IQC}} = \theta(b_R^{\text{I}})$ as maxima at relatively high impact parameters b_R^{I} ($[d\theta(b)/db]_{b=b_R^{\text{I}}} = 0$; cf. Table 2; the superscript: QC indicates the angles' calculation from quasi-classical CS trajectories in Eq. (13)). From the $[90^\circ, 0^\circ]$ orientation, the scattering angle function $\theta(b)$ becomes decreasing at impact parameters b somewhat lower than b_R^{I} and reaches a zero value: $\theta_G(b_G) = 0^\circ$ at a

finite impact parameter b_G (cf. Table 2). That phenomenon known as glory scattering [47] corresponds to an outgoing projectile that acquires an overall zero deflection from its original traveling direction. Other type of zero and nearly zero scattering angles $\theta_s \rightarrow 0^\circ$, known as small angles [47], always occur from all the orientations at very large impact parameters ($b \rightarrow \infty$, cf. Fig. 5) because those correspond to long projectile–target separations that result in weak interactions. Further away from the glory angle position, where $b < b_G$, the scattering angle functions $\theta(b)$ from the $[90^\circ, 0^\circ]$ orientation finally become sharply increasing. Those observed features in $\theta(b)$ from the $[90^\circ, 0^\circ]$ orientation can be explained in terms of the projectile–target interactions as follows. Due to the symmetry of the initial reactants and of their interaction potential, the three nuclei from the $[90^\circ, 0^\circ]$ orientation remain on the original x – z plane (cf. Fig. 1) throughout the entire scattering process. When $b > b_G$, the projectile experiences a net attraction by the target and ends up on the x – z plane, deflected toward the z -axis, and with a negative deflection function: $\Theta(b) = -\theta(b)$ [47]. On the other hand, when $b < b_G$, the projectile experiences a net repulsion by the target and ends up on the x – z plane, deflected off the z -axis, and with a positive deflection function: $\Theta(b) = \theta(b)$ [47]. At exactly $b = b_G$, the transition from repulsive to attractive interactions takes place and provokes a glory scattering with zero deflection function: $\Theta_G(b) = \theta_G(b) = 0^\circ$ [47]. Within the attractive interval: $(b_G, +\infty)$, the attraction is the weakest at the highest impact parameters $b \rightarrow +\infty$ (i.e. at long projectile–target separations) but monotonically increases at lower impact parameters b (i.e. at shorter projectile–target separations) and reaches a maximum in strength at b_R^{I} . The primary rainbow angle θ_R^{IQC} as a maximum in the scattering angle function $\theta(b)$ at b_R^{I} is a manifestation of that maximum in the projectile–target net attraction. As soon as $b < b_R^{\text{I}}$, the net attraction begins to decrease, eventually becomes zero at exactly $b = b_G$, and finally reverts into a net repulsive interaction when $b < b_G$. Comparing in Fig. 5 the scattering angle function $\theta(b)$ from the $[90^\circ, 0^\circ]$ orientation with those from the $[90^\circ, 45^\circ]$ and $[90^\circ, 90^\circ]$ ones, it is discernible that primary rainbow angles are also present from the last two orientations but with increasingly higher values θ_R^{IQC} and at increasingly lower impact parameters b_R^{I} (cf. Table 2). More importantly, the zero glory

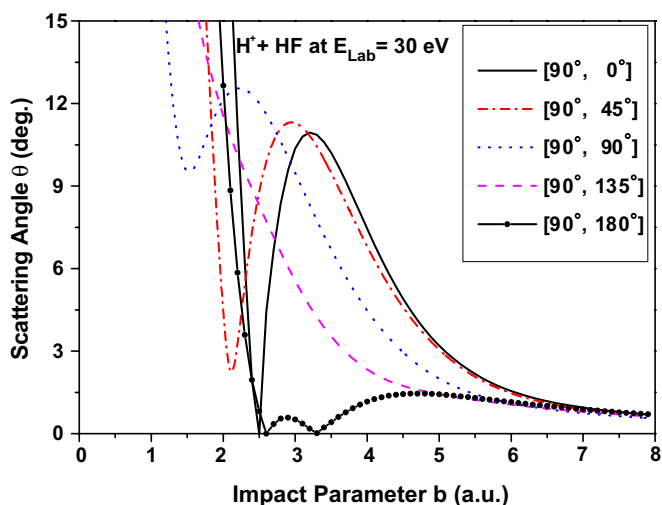


Fig. 5. Scattering angle function $[\theta(b)]$ vs. impact parameter (b) per simulated $[\alpha, \beta]$ orientation.

Table 2

Primary (quasi-classical and uniform Airy-treated) and secondary (quasi-classical) rainbow scattering angles, and positions of glory scattering angles from different target orientations $[\alpha, \beta]$

Orientations $[\alpha, \beta]$ ($^\circ$)	Primary rainbow angles			Secondary rainbow angles		Glory angles ($\theta_G = 0^\circ$)
	Impact parameter, b_R^{I} (a.u.)	Rainbow angle (quasi-classical), θ_R^{IQC} ($^\circ$)	Rainbow angle (uniform Airy-treated), θ_R^{IUAiry} ($^\circ$)	Impact parameter, b_R^{II} (a.u.)	Rainbow angle (quasi-classical, θ_R^{IIQC} ($^\circ$))	Impact parameter, b_G (a.u.)
$[90, 0]$	3.2	10.9	8.8	–	–	2.5
$[90, 45]$	2.9	11.3	9.3	2.1	1.6	–
$[90, 90]$	2.2	12.6	10.7	1.5	9.4	–
$[90, 135]$	–	–	–	–	–	–
$[90, 180]$	4.7	1.5	–	2.9	0.6	2.6 and 3.3

scattering angle $\theta_G(b_G) = 0^\circ$ from the $[90^\circ, 0^\circ]$ orientation is substituted in the other two simulations for secondary rainbow angles $\theta_R^{\text{IIQC}} = \theta(b_R^{\text{II}})$ that are minima in the scattering angle functions at relatively low impact parameters b_R^{II} ($[d\theta(b)/db]_{b=b_R^{\text{II}}} = 0$, cf. Fig. 5). Secondary rainbow angles were first predicted theoretically in the $\text{H}^+ + \text{H}_2$ system by Giese et al. [48] and later corroborated in the same system by the Toennies group [12], both theoretically and experimentally. More significantly, secondary rainbow angles were also predicted in previous END simulations of the $\text{H}^+ + \text{H}_2$ [23,24] and $\text{H}^+ + \text{C}_2\text{H}_2$ [27] systems *inter alia*. From the $[90^\circ, 45^\circ]$ and $[90^\circ, 90^\circ]$ orientations, the lower symmetry in the initial conditions with respect to those from the $[90^\circ, 0^\circ]$ one causes the nuclei not to remain on the original x - z plane but scatter off that plane. A secondary rainbow corresponds to a maximum in that off-plane scattering. Notice that in the case of more symmetric, $\text{D}_{\infty\text{h}}$ targets (e.g. H_2 [23,24] and C_2H_2 [27]), the $[90^\circ, 90^\circ]$ orientation did not lead to an off-plane scattering so that the secondary rainbow effect did not occur there but a glory scattering instead. In all the END-CSD investigated systems including the present one, secondary rainbows are always smaller than primary ones ($\theta_R^{\text{IIQC}} < \theta_R^{\text{IQC}}$) and occurred at lower impact parameters ($b_R^{\text{II}} < b_R^{\text{I}}$). The features of the scattering angle functions $\theta(b)$ from the $[90^\circ, 45^\circ]$ and $[90^\circ, 90^\circ]$ orientations can be explained in terms of repulsive and attractive projectile–target interactions, quite similarly to the previous ones from the $[90^\circ, 0^\circ]$ orientation.

An important effect, clearly discernible in Fig. 5, is that both the values of primary rainbow θ_R^{IQC} and secondary rainbow/glory $\theta_R^{\text{IIQC}}/\theta_G$ angles and the values of their corresponding impact parameter b_R^{I} and b_R^{II}/b_G get closer and closer as β adopts the values: 0° , 45° and 90° . At some value of β : $90^\circ < \beta < 135^\circ$ not presently simulated, the approaching primary (maximum) and secondary (minimum) rainbow angles finally coalesce into an inflexion point so their maximum and minimum features vanish. The precise orientation from which those rainbow angles coalesce was clearly discerned in a previous END-CSD investigation of the $\text{H}^+ + \text{C}_2\text{H}_2$ system [27] because it included far more initial target orientations. In the present system, that coalescence should happen from a not-simulated orientation $[90^\circ, \beta]$ with $90^\circ < \beta < 135^\circ$ to be determined in future investigations. The results from the $[90^\circ, 135^\circ]$ orientation are beyond that rainbow angles coalescence and display no visible rainbow features (cf. Fig. 5). As was the case with the $\text{H}^+ + \text{C}_2\text{H}_2$ system [27], further increase in the azimuthal angle β from the non-rainbow interval ultimately bring back the rainbow features. Thus, the scattering angle function $\theta(b)$ from the $[90^\circ, 180^\circ]$ orientation displays again rainbow angles but in a more complicated pattern that exhibits: (I) a maximum primary rainbow angle at high impact parameters, (II) a maximum (not minimum) secondary rainbow angle at lower impact parameters, and (III) two glory scattering angles (cf. Fig. 5). By continuity, several not-simulated orientations

between $[90^\circ, 90^\circ]$ and $[90^\circ, 135^\circ]$, and between $[90^\circ, 135^\circ]$ and $[90^\circ, 180^\circ]$ should display rainbow angle features as well. The values of the scattering angle functions $\theta(b)$ at relatively high impact parameters (e.g. $b > 4.0$ a.u.) from the $[90^\circ, 0^\circ]$ and $[90^\circ, 45^\circ]$ orientations are clearly greater than their homologous ones from the $[90^\circ, 135^\circ]$ and $[90^\circ, 180^\circ]$ ones. This fact reveals that the net attractive projectile–target interaction at long separations is stronger whenever the H^+ approaches the partially negative F terminus of the $\text{H}^{+\delta}\text{-F}^{-\delta}$ molecule rather than the partially positive H terminus as expected. Rainbow and glory scattering angles manifest experimentally in some conspicuous features in the differential cross section as discussed below.

4.3. Total differential cross section

The most important result from the Toennies group experiments on the $\text{H}^+ + \text{HF}$ system at $E_{\text{Lab}} = 30$ eV is its total differential cross section (DCS) for the combined NCTS and CTS processes. The quantum inelastic DCS $[d\sigma(\theta)/d\Omega]_{i \rightarrow f}$ from initial (i) to the final (f) eigenstates ($i \rightarrow f$) is [47]

$$\begin{aligned} \left[\frac{d\sigma(\theta)}{d\Omega} \right]_{i \rightarrow f} &= \frac{k_f}{k_i} |f_{i \rightarrow f}(\theta)|^2 \\ &= \frac{1}{4k_i^2} \left| \sum_{l=0}^{\infty} (2l+1) T_{\text{Quantum}}^{i \rightarrow f}(l) P_l(\cos \theta) \right|^2 \end{aligned} \quad (14)$$

where $f_{i \rightarrow f}(\theta)$ is the scattering amplitude, k_f (k_i) the projectile initial (final) wave vector, l orbital angular momentum quantum numbers, $T_{\text{Quantum}}^{i \rightarrow f}(l)$ the T-matrix, and $P_l(\cos \theta)$ Legendre polynomials. In the present END-CSD context, the DCS given by Eq. (14) should be reformulated in terms of the CS theory. The complete rigorous derivation of our own CS DCS will be published soon [33,49] but its more relevant outcomes are discussed in detail below. Quite succinctly, our CS DCS theory exploits basic CS properties, implicates Eqs. (6) and (14) *inter alia*, and utilizes different semiclassical techniques to evaluate the sum in Eq. (14). When the scattering angle function $\theta(b)$ is not close to rainbow angles maxima/minima, the CS DCS $[d\sigma(\theta)/d\Omega]_{i \rightarrow f}^{\text{CS}}$ is

$$\begin{aligned} \left[\frac{d\sigma(\theta)}{d\Omega} \right]_{i \rightarrow f}^{\text{CS}} &= \left| \sum_{m=1}^N f(\theta)_m \right|^2 \\ &= \left| \sum_{m=1}^N \frac{\sqrt{b_m} T_{\text{CS}}^{i \rightarrow f}(b_m)}{\sqrt{\sin[\theta(b_m)] \left[\frac{d\theta(b)}{db} \right]_{b=b_m}}} \right|^2, \end{aligned} \quad (15)$$

where the relationships: $l \approx k_i b$ and $T_{\text{Quantum}}^{i \rightarrow f} = T_{\text{CS}}^{i \rightarrow f}$ are used. The stationary phase approximation [40] in the semiclassical limit of $\hbar \rightarrow 0$ for the nuclei is applied at one of the steps leading from Eqs. (14) and (15) in the evaluation of the sum in Eq. (14) as an approximated integral; therefore, the resulting equation (15) contains N stationary quasi-classical trajectories (branches) starting from the impact

parameters b_m ($1 \leq m \leq N$) and ending up with the outgoing projectile scattered into the same direction θ . The maximum number of those stationary quasi-classical trajectories from the presently simulated orientations are: $N = 3$ from $[90^\circ, 0^\circ]$, $[90^\circ, 45^\circ]$ and $[90^\circ, 90^\circ]$; $N = 1$ from $[90^\circ, 135^\circ]$; and $N = 5$ from $[90^\circ, 180^\circ]$, respectively (cf. Fig. 5). The CS action S_{CS} in the phase of $T_{CS}^{i \rightarrow f}$ [cf. Eq. (6)] provokes quantum interference patterns (oscillations) in the CS DCS of Eq. (15) through its coherent sum over quasi-classical trajectory contributions. If that sum is performed incoherently, a (predominantly) quasi-classical DCS $[d\sigma(\theta)/d\Omega]_{i \rightarrow f}^{QC}$ is obtained:

$$\left[\frac{d\sigma(\theta)}{d\Omega} \right]_{i \rightarrow f}^{QC} = \sum_{m=1}^N \frac{b_m |T_{CS}^{i \rightarrow f}(b_m)|^2}{\sin \theta \left| \left[\frac{d\theta(b)}{db} \right]_{b=b_m} \right|}. \quad (16)$$

Although quantum probabilities are still retained in the $|T_{CS}^{i \rightarrow f}(b_m)|^2$ term of Eq. (16), the properties of that quasi-classical DCS are strongly dependent upon quasi-classical trajectory data (e.g. $\theta(b)$, $[d\theta(b)/db]_{b=b_m}$, etc.) and is therefore irreparably plagued with unphysical classical singularities not observed experimentally. In addition, a quasi-classical DCS does not exhibit quantum interference patterns (oscillation) due to its incoherent sum evaluation (the $T_{CS}^{i \rightarrow f}(b_m)$ terms in Eq. (16) lose their phases through the modulus operation). The quasi-classical DCS is the lowest-level approximation to the experimental DCS. Both CS and quasi-classical DCS in Eqs. (15) and (16), respectively, exhibit unphysical singularities, not observed experimentally, at the primary and secondary rainbow angles directions ($\theta = \theta_R^{I, QC}$ and $\theta_R^{II, QC}$) because their denominator terms: $[d\theta(b)/db]_{b=b_m}$ becomes zero when $b = b_R^I$ and b_R^{II} . The reason for that failure arises from the fact that near a rainbow angle direction at least two quasi-classical trajectories contributing to the DCS become extremely close and even finally merge into one single trajectory at exactly the rainbow angle direction. Whenever two or more trajectories become very close, the simple stationary phase approximation, implicit in Eqs. (15) and (16), is no longer valid. That limitation rules out both Eqs. (15) and (16) in the calculation of DCS near and at the rainbow angles direction. More advanced semiclassical techniques should be applied to Eq. (14) to obtain non-singular CS DCS near rainbow angles. For instance, the uniform Airy approximation [47,50] is the most rigorous semiclassical treatment of an isolated rainbow angle singularly that occurs when only two of the trajectories contributing to the DCS become very close. That relatively simple case happens herein from the $[90^\circ, 0^\circ]$ orientation (cf. Fig. 5). In more complex situations, the uniform Pearcey approximation [50] is the most rigorous semiclassical treatment of two adjacent rainbow angles (herein, primary and secondary ones) that occur when three of the trajectories contributing to the DCS become very close. That more complex case happens herein from the $[90^\circ, 45^\circ]$, $[90^\circ, 90^\circ]$ and $[90^\circ, 180^\circ]$ orientations (cf. Fig. 5). However, the uniform Pearcey approximation

is extremely cumbersome to apply within the present CS context. Previous studies of the $H^+ + H_2$ [24], $H^+ + CH_4$ [25], $H^+ + H_2O$ [26], and $H^+ + C_2H_2$ [27] systems firmly demonstrated that the singularities of primary rainbow angles are far sharper than those of secondary ones so that accurate DCS can be obtained by applying the simpler uniform Airy approximation only to the primary rainbow angles and by leaving the inconspicuous secondary angle singularity untreated [50]. With the uniform Airy approximation, the two contributions to the DCS in Eq. (15) by two close attractive trajectories with $m = 2$ and 3 near the rainbow angle singularity is replaced by a single scattering amplitude $f_{23}^{U, Airy}(\theta)$:

$$f_{23}^{U, Airy}(\theta) = \pi^{1/2} \exp \left[i(A_{23} - \frac{1}{4}\pi) \right] \left\{ \left[\left| \frac{d\sigma(\theta)}{d\Omega} \right|_2^{1/2} + \left| \frac{d\sigma(\theta)}{d\Omega} \right|_3^{1/2} \right] \xi_{23}^{1/4} Ai(-\xi_{23}) - i \left[\left| \frac{d\sigma(\theta)}{d\Omega} \right|_2^{1/2} - \left| \frac{d\sigma(\theta)}{d\Omega} \right|_3^{1/2} \right] \xi_{23}^{-1/4} Ai'(-\xi_{23}) \right\}, \quad (17)$$

where $A_{23}(\theta)$ and $\xi_{23}(\theta)$ [50] are functions of the CS actions S_{CS} along the two close trajectories, and $Ai()$ and $Ai'()$ are the Airy function and its first derivative. With Eq. (17), the quasi-classical primary rainbow angle singularity is replaced by and shifted to the first bounded maximum of the Airy function [50]. The uniform Airy CS DCS goes uniformly to the simpler CS DCS of Eq. (15) when θ is away from the rainbow angle value and to a transitional Airy approximation [50] CS DCS when θ is close to that rainbow angle value. It is worth noticing that Eqs. (15)–(17) also exhibit unphysical singularities at glory and small scattering angles because their ubiquitous denominator term: $\sin \theta$ approach zero whenever $\theta \approx 0^\circ$. Semiclassical treatments for those types of singularities are well-known [47] and have been reformulated for the present CS context as well [33,49]. However, those refinements are unnecessary herein because the measured DCS in the $H^+ + HF$ system never reached a scattering angle θ below 1° .

Calculated total NCTS/CTS CS DCS for the $H^+ + HF$ system at $E_{Lab} = 30\text{eV}$. and from the simulated $[90^\circ, 0^\circ]$ orientation are shown in Fig. 6, both at the quasi-classical (Eq. (16)) and the uniform Airy (Eq. (17)) levels, along with the experimental result. The last one was reported un-normalized but in Fig. 6, it has been normalized to match the uniform Airy CS DCS. The quasi-classical DCS shows a conspicuous rainbow angle singularly at $\theta = \theta_R^{I, QC} = 10.9^\circ$ that is notably absent in its uniform Airy and experimental counterparts. Except for that blemish, the quasi-classical DCS agrees acceptably with the measured result. On the other hand, the uniform Airy CS DCS agrees extremely well with the experimental result in regard to shape and features. That individual uniform Airy CS DCS from the $[90^\circ, 0^\circ]$ orientation exhibits perceptible interference and supernumerary rainbow angles patterns (oscillations) that are far more prominent than those in the experimental

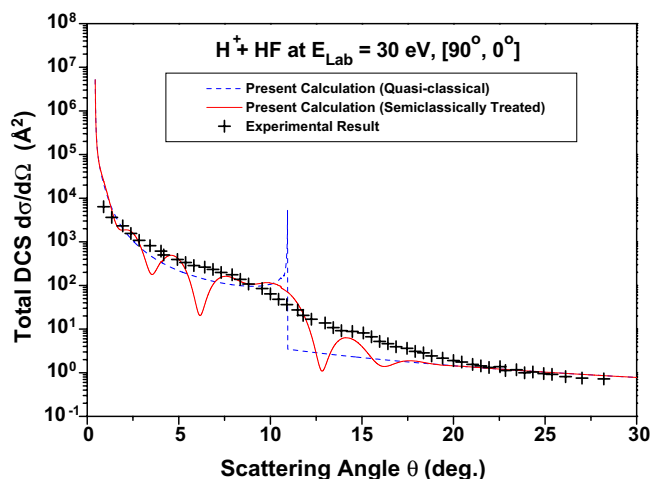


Fig. 6. $H^+ + HF$ total NCTS/CTS differential cross sections $[d\sigma(\theta)/d\Omega]$ vs. scattering angle (θ) from the $[90^\circ, 0^\circ]$ orientation: quasi-classical, uniform Airy-treated and experimental results.

result. This is so because the experimental DCS collects contributions by several DCS resulting from all possible target orientations. That “experimental averaging” somewhat blurs the quantum interference patterns. As explained above, the uniform Airy approximation is also applied to the primary rainbow angle singularities from the $[90^\circ, 45^\circ]$ and $[90^\circ, 90^\circ]$ orientations in a similar way as that done in the $[90^\circ, 0^\circ]$ one, and produce similar results. From those three orientations, the quasi-classical primary rainbow singularity is substituted by and shifted to the first bounded maximum of the Airy function. That first maximum corresponds to an Airy-treated rainbow-angle bounded peak that occurs at scattering angles θ_R^{Airy} that are always smaller than their quasi-classical counterparts θ_R^{QC} . The rainbow angles for those three considered orientations are successively (cf. Table 2): 10.9° ($[90^\circ, 0^\circ]$), 11.3° ($[90^\circ, 45^\circ]$) and 12.6° ($[90^\circ, 90^\circ]$) in the quasi-classical case; and 8.7° ($[90^\circ, 0^\circ]$), 9.2° ($[90^\circ, 45^\circ]$) and 10.6° ($[90^\circ, 90^\circ]$) in the Airy-treated one. The latter values are about 2° smaller than their quasi-classical counterparts and agree satisfactorily with the experimentally inferred rainbow angle of 8° [14]. However, a more meaningful comparison of rainbow angles should be done with the finally predicted DCS (see below) because the plain values of those angles do not take into account their individual weights through their DCS intensities in the final DCS.

Unlike the three previous orientations, the pattern in the scattering angle function $\theta(b)$ from the $[90^\circ, 180^\circ]$ orientation poses some difficulties to a DCS calculation. This orientation exhibits two very low rainbow angles of 1.5° (primary) and 0.6° (secondary), respectively (cf. Table 2 and Fig. 5), that lie at the lower limit of applicability of the uniform Pearcey and Airy approximations [50] (as a rough estimate, those approximations can not be employed at scattering angles smaller than 1° – 2°). In addition, those rainbow angles are very close to two glory angles (cf. Table 2 and Fig. 5). Therefore, a proper treatment of those rain-

bow angles would require a combined semiclassical technique capable of dealing simultaneously with contiguous rainbow, glory and small angles. To the best of our knowledge, that complex technique does not exist and a CS DCS free of unphysical singularities can not be calculated from the $[90^\circ, 180^\circ]$ orientation. On the other hand, the CS DCS from the $[90^\circ, 135^\circ]$ orientation is the simplest to evaluate because its scattering angle function $\theta(b)$ does not exhibit any rainbow angles features (cf. Fig. 5). Therefore, the $[90^\circ, 135^\circ]$ CS DCS contains only one branch ($N=1 \Rightarrow m=1$) that renders a plain quasi-classical DCS free of rainbow singularities:

$$\left[\frac{d\sigma(\theta)}{d\Omega} \right]_{i \rightarrow f}^{\text{QC}} = \frac{b_1 |T_{\text{CS}}^{i \rightarrow f}(b_1)|^2}{\sin \theta \left| \left[\frac{d\theta(b)}{db} \right]_{b=b_1} \right|}; \quad [90^\circ, 135^\circ]. \quad (18)$$

The finally predicted total NCTS/CTS CS DCS for the $H^+ + HF$ system at $E_{\text{Lab}} = 30$ eV as an average over the $[90^\circ, 0^\circ]$, $[90^\circ, 45^\circ]$ and $[90^\circ, 90^\circ]$ orientations results is shown in Fig. 7 at the quasi-classical uniform Airy level [Eq. (17)] in comparison with the experimental result. As before, this last result has been normalized in Fig. 7 to match the theoretical DCS. The predicted uniform Airy CS DCS agrees extremely well with the measured DCS in regard to shape and features. More importantly, one of the bounded peaks of the theoretical result shows up around the value of the experimentally inferred rainbow angle of 8° [14]. For the same reasons discussed above, the theoretical DCS exhibits perceptible interference and supernumerary rainbow angles patterns (oscillations) that are far more prominent than those in the measured result. In the finally predicted CS DCS, the contribution from the $[90^\circ, 180^\circ]$ orientation has been obviously excluded from the final average because its not treated singularities would contaminate the final results with unphysical features. The CS DCS from the $[90^\circ, 135^\circ]$ does not exhibit any rainbow

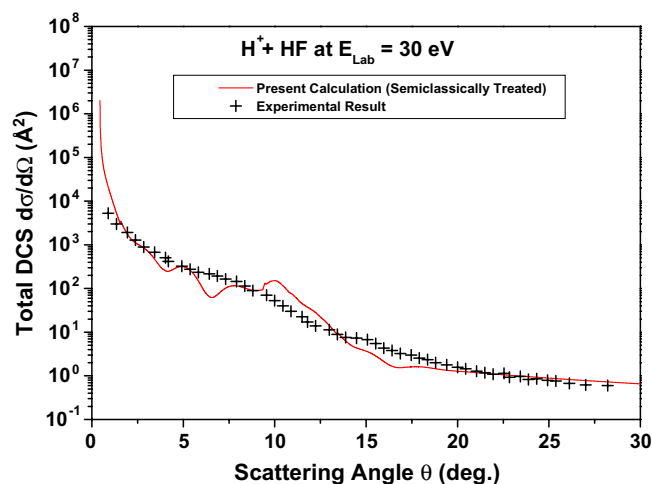


Fig. 7. $H^+ + HF$ average total NCTS/CTS differential cross sections $[d\sigma(\theta)/d\Omega]$ vs. scattering angle (θ): uniform Airy-treated and experimental results.

angle and is therefore free of singularities; however, that lack of rainbow angles produces a rather flat DCS that if included in the average would considerably decrease the genuine rainbow-angle features from the other three orientations. For that reason, the $[90^\circ, 135^\circ]$ CS DCS was excluded from the final result. The CS DCS from that orientation could be safely included in the final average if many more intercalated orientations having rainbow angle features were calculated to outweigh the $[90^\circ, 135^\circ]$ flattening effect (important additional orientations would include those between $[90^\circ, 90^\circ]$ and $[90^\circ, 135^\circ]$, and between the $[90^\circ, 135^\circ]$ and $[90^\circ, 180^\circ]$). Those further simulations will be conducted in the future. At present, the finally predicted total NCTS/CTS CS DCS for the $H^+ + HF$ system at $E_{\text{Lab}} = 30$ eV. from the $[90^\circ, 0^\circ]$, $[90^\circ, 45^\circ]$ and $[90^\circ, 90^\circ]$ orientations reproduce extremely well the measured DCS.

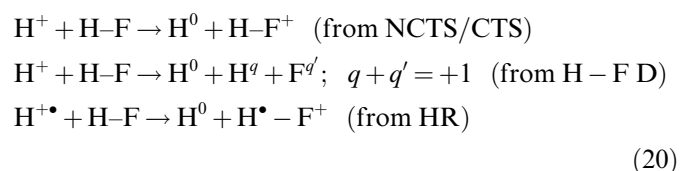
Finally, it should be noticed that a more direct use of the full quantum-mechanical DCS of Eq. (14) without employing semiclassical techniques may circumvent some of the singularity problems encountered in the present DCS calculations. However, that alternative approach was not followed because of two compelling reasons. The first reason is that such a treatment produces DCS that agree well at low scattering angles but considerably deteriorate at high ones [30]. The second reason is that in the present approach, the nuclear motion that critically determines the DCS is described quasi-classically; therefore, a semiclassical treatment of the DCS is the most consistent with a quasi-classical CS description of the nuclei. Furthermore, that semiclassical treatment makes completely transparent the origin of rainbow angle effects from the topology of the quasi-classical CS trajectories.

4.4. Charge-transfer integral cross sections

Integral cross sections (ICS) $\sigma_{i \rightarrow f}$ for a processes starting from initial (i) to final (f) eigenstates ($i \rightarrow f$) are obtained by integrating the corresponding DCS over the solid angle Ω . In the present context, a CS ICS $\sigma_{i \rightarrow f}^{\text{CS}}$ turn out to be [33]:

$$\sigma_{i \rightarrow f} = \int_0^{4\pi} \left[\frac{d\sigma(\Omega)}{d\Omega} \right]_{i \rightarrow f} d\Omega = 2\pi \int_0^\infty P_{\text{CS}}^{i \rightarrow f}(b) b db, \quad (19)$$

where $P_{\text{CS}}^{i \rightarrow f}(b) = |T_{\text{CS}}^{i \rightarrow f}(b)|^2$ is the CS transition probability for the process $i \rightarrow f$. An important property to characterize the $H^+ + HF$ reactive system is the one-electron charge-transfer reaction (CTR) ICS $\sigma_{\text{CTR}}^{\text{CS}}$ that collects contributions from the three predicted reactions:



In each contributing reaction, the probability in Eq. (19) is $P_{\text{CS}}^{i \rightarrow f} = P_{\text{CS}}^{\text{CTR}} \propto |A_e^{i \rightarrow f}|^2$ (cf. Eq. (6)), which is directly related

to the electronic Mulliken population of the fastest outgoing projectile H^q as rigorously proven elsewhere [33]. A “direct” CTR ICS is due to the NCTS/CTS reaction alone whereas a “complete” CTR ICS is due to both “direct” and “indirect” contributions (i.e. from H-F D and HR). In the latter case, the final fastest outgoing projectile $H^{q=0}$ carrying one electron is not (may not be) the same as the original projectile H^+ in the HR(H-F D) reaction. The calculated END-CSD/pVDZ one-electron CTR ICS $\sigma_{\text{CTR}}^{\text{CS}}$ are: $3.36 \times 10^{-5} \text{ \AA}^2$ (“direct” CTR) and 0.07 \AA^2 (“complete” CTR). There are no experimental σ_{CTR} to compare with but similar $\sigma_{\text{CTR}}^{\text{CS}}$ calculations in the $H^+ + CH_4$ [25] and $H^+ + C_2H_2$ [27] systems agree well with available experimental results.

5. Concluding remarks

The results of this complete study of $H^+ + HF$ system at $E_{\text{Lab}} = 30$ eV show that the END-CSD/pVDZ theory employing (I) frozen Gaussian wave packets for the nuclei and (II) a single-determinantal Thouless CS for the electrons can adequately describe the system reactivity and accurately predict its dynamical properties. In particular, the calculated total differential cross section shows an excellent agreement with the available experimental result.

Acknowledgments

Mr. Anthony Austin was a 2006 Welch Summer Scholar. The authors are indebted to the Robert A. Welch Foundation for its generous support to Mr. Austin's undergraduate research at Texas Tech University. All the present calculations have been conducted at the Texas Tech University High Performance Computer Center, to which generous use of computer time and technical support are gratefully acknowledged. This material is based upon work partially supported by the National Science Foundation under Grant CHE-0645374 (CAREER), by the Robert A. Welch Foundation under Grant D-1539, and by an award from the Research Corporation. Also, acknowledgement is made to the donors of The American Chemical Society Petroleum Research fund for partial support of this research.

References

- [1] J.B. Hasted, *Adv. At. Mol. Phys.* 15 (1979) 205.
- [2] H. Udseth, C.F. Giese, W.R. Gentry, *Phys. Rev. A* 8 (1973) 2483.
- [3] R. Schinke, H. Krüger, V. Hermann, H. Schmidt, F. Linder, *J. Chem. Phys.* 67 (1977) 1187.
- [4] H. Schmidt, V. Hermann, F. Linder, *J. Chem. Phys.* 69 (1978) 2734.
- [5] V. Hermann, H. Schmidt, F. Linder, *J. Phys. B* 11 (1978) 493.
- [6] G. Krutein, G. Bischof, F. Linder, R. Schinke, *J. Phys. B* 12 (1979) L57.
- [7] T. Kusakabe, K. Asahina, A. Iida, Y. Thanaka, Y. Li, G. Hirsch, R.J. Buenker, M. Kimura, H. Tawara, Y. Nakai, *Phys. Rev. A* 62 (2000) 062715.
- [8] S. Cheng, Y. Liu, *J. Phys. B* 32 (1999) 825.

- [9] J.M. Sanders, S.L. Varghese, C.H. Fleming, G.A. Soosai, *J. Phys. B* 36 (2003) 3835.
- [10] S.L. Varghese, G. Bissinger, J.M. Joyce, R. Laubert, *Phys. Rev. A* 31 (1985) 2202.
- [11] W.E. Wilson, L.H. Toburen, *Phys. Rev. A* 11 (1975) 1303.
- [12] G. Neidner, M. Noll, J.P. Toennies, C. Schlier, *J. Chem. Phys.* 87 (1987) 2685.
- [13] M. Noll, J.P. Toennies, *J. Chem. Phys.* 85 (1986) 3313.
- [14] B. Friedrich, F.A. Gianturco, G. Niedner, M. Noll, J.P. Toennies, *J. Phys. B* 20 (1987) 3725.
- [15] B. Friedrich, G. Neidner, M. Noll, J.P. Toennies, *J. Chem. Phys.* 87 (1987) 5256.
- [16] G. Niedner, M. Noll, J.P. Toennies, *J. Chem. Phys.* 87 (1987) 2067.
- [17] N. Aristov, G. Niedner Schatteburg, J.P. Toennies, Y. Chiu, *J. Chem. Phys.* 95 (1991) 7969.
- [18] U. Gierz, M. Noll, J.P. Toennies, *J. Chem. Phys.* 83 (1985) 2259.
- [19] Y. Chiu, B. Friedrich, W. Maring, G. Niedner, M. Noll, J.P. Toennies, *J. Chem. Phys.* 88 (1988) 6814.
- [20] J.C. Tully, J.K. Preston, *J. Chem. Phys.* 55 (1971) 562.
- [21] M. Baer, G. Niender-Schatterburg, J.P. Toennies, *J. Chem. Phys.* 91 (1989) 4169.
- [22] E. Deumens, A. Diz, R.L. Longo, Y. Öhrn, *Rev. Mod. Phys.* 66 (1994) 917.
- [23] J.A. Morales, A. Diz, E. Deumens, Y. Öhrn, *Chem. Phys. Lett.* 74 (1995) 392.
- [24] J.A. Morales, A. Diz, E. Deumens, Y. Öhrn, *J. Chem. Phys.* 103 (1995) 9968.
- [25] D. Jacquemin, J.A. Morales, E. Deumens, Y. Öhrn, *J. Chem. Phys.* 107 (1997) 6146.
- [26] M. Hedström, J.A. Morales, E. Deumens, Y. Öhrn, *Chem. Phys. Lett.* 279 (1997) 241.
- [27] J.A. Morales, B. Maiti, Y. Yan, K. Tsereteli, J. Laraque, S. Addepalli, C. Myers, *Chem. Phys. Lett.* 414 (2005) 405.
- [28] N. Aristov, G. Niednerschatteburg, J.P. Toennies, Y.N. Chiu, *J. Chem. Phys.* 95 (1991) 7969.
- [29] S.A. Malinovskaya, R. Cabrera-Trujillo, J.R. Sabin, E. Deumens, Y. Öhrn, *J. Chem. Phys.* 117 (2002) 1103.
- [30] Y. Yan, J.A. Morales, *J. Chem. Phys.* (submitted for publication).
- [31] E. Schäfer, R.J. Saykally, *J. Chem. Phys.* 80 (1984) 2973.
- [32] E. Schäfer, R.J. Saykally, *J. Chem. Phys.* 81 (1984) 4189.
- [33] J.A. Morales, in preparation.
- [34] J.R. Klauder, B.S. Skagerstam, *Coherent States Applications in Physics and Mathematical Physics*, World Scientific, Singapore, 1985.
- [35] H. Goldstein, *Classical Mechanics*, Addison-Wesley, Reading, MA, 1980.
- [36] P. Kramer, M. Saraceno, *Geometry of the Time-Dependent Variational Principle in Quantum Mechanics*, Springer, New York, 1981.
- [37] J.A. Morales, E. Deumens, Y. Öhrn, *J. Math. Phys.* 40 (1999) 766.
- [38] D.J. Thouless, *Nucl. Phys.* 21 (1960) 225.
- [39] E. Deumens, Y. Öhrn, B. Wiener, *J. Math. Phys.* 32 (1991) 1166.
- [40] J.A. Morales, Ph.D. Thesis, University of Florida, 1997.
- [41] K. Tsereteli, Y. Yan, J.A. Morales, *Chem. Phys. Lett.* 420 (2006) 54.
- [42] K. Tsereteli, S. Addepalli, J. Perez, J.A. Morales, *Concurring Engineering Research and Applications, Next Generation Concurrent Engineering*, ISPE, Inc., 2005, p. 469.
- [43] I. Foster, *The Grid: Blue Print for a New Computing Infrastructure*, Morgan Kaufman Publishers, San Francisco, CA, 1999.
- [44] T.H. Dunning Jr., *J. Chem. Phys.* 53 (1970) 2823.
- [45] T.H. Dunning Jr., *J. Chem. Phys.* 90 (1989) 1007.
- [46] A. Szabo, N.S. Ostlund, *Modern Quantum Chemistry*, Dover Publications, Inc., Mineola, NY, 1989.
- [47] M.S. Child, *Molecular Collision Theory*, Dover Publications, Inc., Mineola, NY, 1984.
- [48] C. Giese, W.R. Gentry, *Phys. Rev. A* 10 (1974) 2156.
- [49] Y. Yan, B. Maiti, J.A. Morales, in preparation.
- [50] J.N.L. Connor, D. Farrelly, *J. Chem. Phys.* 75 (1981) 2831.